

Time domain simulations of wind- and wave-induced load effects on a three-span suspension bridge with two floating pylons[☆]

Yuwang Xu^{a,*}, Ole Øiseth^a, Torgeir Moan^{b,c}

^a Department of Structural Engineering, Norwegian University of Science and Technology (NTNU), Norway

^b Centre for Ships and Ocean Structures (CeSOS), NTNU, Norway

^c Centre for Autonomous Marine Operations and Systems (AMOS), NTNU, Norway

ARTICLE INFO

Keywords:

Suspension bridge
Floating pylon
Wind load
Wave load

ABSTRACT

The construction of a three-span suspension bridge with two floating pylons is currently being considered for crossing the 5-km-wide and 550-m-deep Bjørnafjorden in Norway. The bridge design represents a novel concept that requires a detailed dynamic analysis to improve the current understanding of its dynamic behavior. Geometric nonlinearities in the cables and mooring system and nonlinearities in the load models are of particular interest; in addition, the relative influence of the buffeting wind forces and the first- and second-order wave excitation forces were carefully studied. The response predictions were obtained using state-of-the-art time domain methods.

1. Introduction

The Norwegian Public Roads Administration is administering a project—Ferry free coastal route E39—which aims to eliminate all ferries along the coastal highway E39 in Norway. One of the straits, Bjørnafjorden, is up to 5 km wide and 0.5 km deep, calling for a significant extension of current bridge technology. A three-span suspension bridge with two floating pylons, a combination of off-shore and bridge technology, is a new concept for crossing wide and deep fjords [1,2]. The bridge represents an entirely new design, requiring a detailed analysis of its dynamic behavior. Time domain methods are commonly applied when nonlinearities must be considered, as it is challenging to include such nonlinearities in a frequency domain analysis. Thus, assessing the influence of nonlinearities in the model is of particular interest to determine whether the calculations must be performed in the time domain or if the faster frequency domain methods are sufficient.

Modeling the motion-induced forces is a major challenge in the time domain simulations of the dynamic response, as they are dependent on the motion history. It is convenient to model the self-excited force in the time domain based on quasi-steady theory [3] and use coefficients from static wind tunnel experiments because the coefficients in quasi-steady theory are not dependent on the frequency; however, it can be challenging to accurately model the self-excited forces using quasi-steady theory, which has resulted in a number of suggestions for improvements [4,5]. The fluid memory effect can be considered by transfer functions in the frequency domain or by convolution integrals in the time domain. The self-excited forces for bridge decks are commonly modeled in the frequency domain using flutter derivatives, as proposed by Scanlan and coworkers [6]. The flutter derivatives represent an empirical generalization of the analytical expressions of the self-excited forces for airfoils (i.e., Theodorsen's function) [7]. The Wagner function [8,9] is the time domain counterpart to Theodorsen's function, and this work has also been generalized for bridge applications. Time

[☆] Editor of this paper: John Niedzwecki, Texas A&M University, College Station, Texas, USA.

* Corresponding author.

E-mail address: yuwang.xu@ntnu.no (Y. Xu).

domain simulations of self-excited forces for bridge applications commonly start with an empirical expression for the transfer function in the frequency domain or the indicial functions in the time domain. The challenge is to fit the various models to the experimental data of the aerodynamic derivatives. The most common approach is perhaps the use of rational functions, also known as Roger's approximation [10]. The majority of the aforementioned studies were either limited by simplified systems using still-air modes as generalized coordinates or detailed studies of the performance of the methodology considering a bridge deck section model. In bridge design, it is necessary to include self-excited forces in a finite element analysis of the entire bridge. Borri et al. [11] expressed the self-excited forces in the time domain by indicial functions and implemented the methodology in the finite element code FEMAS. Salvatori and Spinelli [12] also simulated the self-excited forces by convolution integrals using indicial functions, developed a finite element program capable of handling simplified bridge models, and analyzed the effects of structural nonlinearities and wind coherence. Chen et al. [13,14] used a state-space model to simulate the fluid memory effect, which can be more computationally efficient than solving the convolution integrals. Additionally, nonlinear effects were carefully studied in a flutter and buffeting analysis in the time domain. Øiseth et al. [15] also applied a state-space model of a simple beam with properties similar to a long-span bridge, and state variables were included as additional degrees of freedom in each node of a beam element.

The hydrodynamic radiation forces are similar to the aerodynamic self-excited forces in that they also depend on the motion history. The most convenient approach is to replace the frequency-dependent added mass and damping by constant coefficients, which are chosen at a dominating frequency, for instance, the peak frequency of the wave or the natural frequency of the structural system. However, this simple method cannot provide accurate results in the analysis of the structures' transient response under a single frequency excitation or the steady-state response under multiple frequency excitations [16]. Cummins' equation is widely used for time domain simulations of structures interacting with water to consider the frequency-dependent characteristics [17]. This equation is a vector integro-differential equation that involves convolution terms that account for the fluid memory effect and has been applied by many researchers [18,19]. However, it is time consuming to solve the convolution integrals during a dynamic analysis [15,20], and replacing the convolution integral with a state-space model is an attractive alternative. Taghipour et al. [20] verified that the same accuracy as obtained by solving Cummins equation directly can be obtained by replacing the convolution integral with a state-space model, and the calculations are approximately eight times faster. They also validated the methodology by comparing their results to experimental data for a flexible barge [21]. The state-space model has also been used by many researchers in different areas [22,23].

As outlined above, state space models are commonly used in the modeling of both hydrodynamic and aerodynamic self-excited forces. However, there are few studies on the performance of the methodology for modeling the dynamic behavior of structures subjected to both wind and wave actions. Thus, this paper provides a brief introduction to the state space modeling of self-excited aerodynamic and radiation forces; a description of the inclusion of state space models in a finite element model of a three-span suspension bridge with two floating pylons is provided. Studies on the dynamic behavior of the bridge consider first- and second-order wave excitations as well as the mean wind and linear and nonlinear buffeting forces. The influence of the nonlinear effects on the models is also carefully studied in order to present some general trends of what is important to include in the modeling of this novel bridge concept.

2. Dynamic response of a suspension bridge with floating pylons

Fig. 1 shows a three-span suspension bridge with two floating pylons crossing Bjørnafjorden in Norway. The main cables are supported by two fixed pylons at each end of the bridge and two floating pylons in the middle of the bridge. The bottom part of the floating pylon is similar to tension leg platforms moored by four groups of tethers, providing a high stiffness in heave, pitch and roll. The water depth is 550 m and 450 m at the left and right floating pylons, respectively. To assess the dynamic behavior of the bridge, it is necessary to consider wind loading on the girder and pylons as well as wave loads on the floating pylons. The equation of motion can be written as

$$\mathbf{M}_s \ddot{\mathbf{u}}(t) + \mathbf{C}_s \dot{\mathbf{u}}(t) + (\mathbf{K}_s + \mathbf{K}_h) \mathbf{u}(t) = \underbrace{\mathbf{F}_{mean} + \mathbf{F}_{Buff}(t) + \mathbf{F}_{se}(t)}_{\mathbf{F}_{Aero}} + \underbrace{\mathbf{F}_{WA}^{(1)}(t) + \mathbf{F}_{WA}^{(2+)}(t) - \mathbf{F}_{Rad}(t)}_{\mathbf{F}_{Hydro}} \quad (1)$$

here, \mathbf{M}_s , \mathbf{C}_s and \mathbf{K}_s symbolize the still-air mass, damping and stiffness matrix, respectively, and \mathbf{u} represents the degrees of freedom



Fig. 1. Three-span suspension bridge with two floating pylons. Illustrated by Arne Jørgen Myhre, Statens vegvesen.

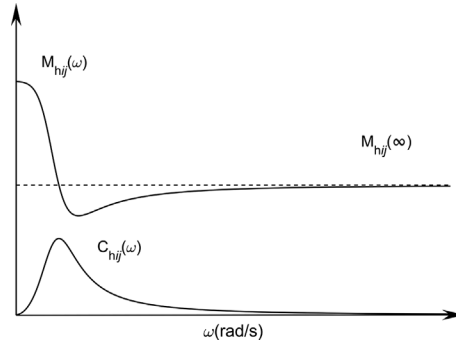


Fig. 2. Typical frequency-dependent added mass and damping coefficients.

of the finite element model. \mathbf{F}_{Aero} represents the wind actions, which consist of a time-invariant component \mathbf{F}_{mean} due to the mean wind velocity, a dynamic component \mathbf{F}_{Bufl} due to turbulence in the wind field and self-excited forces \mathbf{F}_{se} generated by the motion of the girder. \mathbf{F}_{Hydro} represents the wave actions, which consist of the radiation forces \mathbf{F}_{Rad} induced by the motion of the submerged part of the pylons, the hydrostatic restoring stiffness \mathbf{K}_h , and the first- and second-order wave excitation forces, $\mathbf{F}_{WA}^{(1)}$ and $\mathbf{F}_{WA}^{(2\pm)}$. Viscous drag damping forces on the submerged part of the floating pylons have not been considered since the aerodynamic damping is significant in the low frequency range where the hydrodynamic potential damping is close to zero. Possible excitations due to vortex shedding are out of the scope of this study, but are relevant for the design of the bridge girder, hangers and tethers. Possible vortex induced motions of the pylons might also be of relevance. We will describe the methods used to model the wind and wave forces in this chapter, with a particular focus on modeling the motion-induced forces in an efficient manner in the time domain to reduce the computational effort required.

2.1. Efficient modeling of motion-induced forces

2.1.1. Radiation forces

When a floating structure oscillates in waves or still water, it generates outgoing waves, resulting in oscillating fluid pressures on the surface of the body [24]. The integrated hydrodynamic pressures give rise to radiation forces, which are defined as follows for a single-frequency motion:

$$\mathbf{F}_{Rad} = \mathbf{M}_h(\omega)\ddot{\mathbf{u}} + \mathbf{C}_h(\omega)\dot{\mathbf{u}} \quad (2)$$

Here, $\mathbf{M}_h(\omega)$ and $\mathbf{C}_h(\omega)$ represent the frequency-dependent added mass and potential damping matrices, respectively. When the oscillation frequency tends to infinity, the damping converges to zero, whereas the added mass becomes constant and frequency independent, as shown in Fig. 2.

$$\begin{aligned} \mathbf{M}_h(\omega) &= \mathbf{m}_h(\omega) + \mathbf{M}_h(\infty) \\ \mathbf{C}_h(\omega) &= \mathbf{c}_h(\omega) + \mathbf{C}_h(\infty) = \mathbf{c}_h(\omega) \end{aligned} \quad (3)$$

The frequency-dependent added mass and damping are commonly obtained via potential theory, as discussed in the next chapters. The radiation force \mathbf{z}_{Rad} , which only accounts for the frequency-dependent terms $\mathbf{m}_h(\omega)$ and $\mathbf{c}_h(\omega)$, can be expressed in the frequency domain as

$$\mathbf{G}_{z_{Rad}}(\omega) = \mathbf{H}(\omega)\mathbf{G}_{\dot{\mathbf{u}}}(\omega) \quad (4)$$

Here, $\mathbf{H}(\omega)$ is the hydrodynamic transfer function, $\mathbf{H}(\omega) = i\omega\mathbf{m}_h(\omega) + \mathbf{c}_h(\omega)$, and $\mathbf{G}_{z_{Rad}}(\omega)$ and $\mathbf{G}_{\dot{\mathbf{u}}}(\omega)$ represent the Fourier transform of the radiation force and the velocity of the rigid body. By applying the inverse Fourier transform to Eq. (4), the forces can be expressed in the time domain as follows:

$$\mathbf{z}_{Rad}(t) = \int_{-\infty}^{\infty} \mathbf{h}(t - \tau)\dot{\mathbf{u}}(\tau)d\tau \quad (5)$$

Here, $\mathbf{h}(t)$ is the inverse Fourier transform of $\mathbf{H}(\omega)$. Eq. (5) consists of $6 \times 6 = 36$ convolution integrals, and it is time consuming to solve the convolution integrals during a dynamic analysis, as noted by several authors [15,20]. Replacing convolution integrals with state-space models is an efficient alternative. In this chapter, for brevity, we will only consider the convolution integral contributing to the radiation force in the i -direction due to motion in the j -direction, $z_{ij}^{(Rad)}(t) = \int_{-\infty}^{\infty} h_{ij}(t - \tau)\dot{u}_j(\tau)d\tau$, as the other integrals are handled in the same manner.

For a stable linear dynamic system, the relationship between the input $\dot{u}_j(t)$ and the output $z_{ij}^{(Rad)}(t)$ can be characterized by an ordinary differential equation (ODE) with high-order derivatives [20]:

$$\frac{d^n z_{ij}^{(Rad)}(t)}{dt^n} + q_{n-1} \frac{d^{n-1} z_{ij}^{(Rad)}(t)}{dt^{n-1}} + \cdots + q_1 \frac{dz_{ij}^{(Rad)}(t)}{dt} + q_0 z_{ij}^{(Rad)}(t) = p_m \frac{d^m \dot{u}_j(t)}{dt^m} + p_{m-1} \frac{d^{m-1} \dot{u}_j(t)}{dt^{m-1}} + \cdots + p_1 \frac{d\dot{u}_j(t)}{dt} + p_0 \dot{u}_j(t) \quad (6)$$

The transfer function of the system can be obtained by taking the Laplace transform

$$\begin{aligned} Z_{ij}^{(Rad)}(s) &= H'_{ij}(s) \dot{U}_j(s) \\ H'_{ij}(s) &= \frac{p_m s^m + p_{m-1} s^{m-1} + \dots + p_1 s + p_0}{s^n + q_{n-1} s^{n-1} + \dots + q_1 s + q_0} \end{aligned} \quad (7)$$

Here, $Z_{ij}^{(Rad)}(s)$ and $\dot{U}_j(s)$ are the Laplace transforms of $z_{ij}^{(Rad)}(t)$ and $\dot{u}_j(t)$, and $H'_{ij}(s)$ is the transfer function. The relation between the transfer function in the Fourier and Laplace formations is $H'_{ij}(s)|_{s=i\omega} = H_{ij}(\omega)$. The degree of the polynomial in the denominator is often taken as one order higher than that of the polynomial in the numerator, $n = m + 1$. By choosing a proper order and applying the inverse Laplace transform, the relation between the output (radiation force) and input (velocity) in Eq. (6) can be expressed as a state space model, which has been previously described in detail [20]:

$$\begin{cases} \dot{\mathbf{X}}(t) = \mathbf{D}_c^{(H)} \mathbf{X}(t) + \mathbf{E}_c^{(H)} \dot{u}_j(t) \\ z_{ij}^{(Rad)}(t) = \mathbf{Q}_c^{(H)} \mathbf{X}(t) \end{cases} \quad i, j \in \{1, 2, \dots, 6\} \quad (8)$$

where

$$\mathbf{X}(t) = \begin{bmatrix} X_1(t) \\ X_2(t) \\ \vdots \\ X_n(t) \end{bmatrix}, \mathbf{D}_c^{(H)} = \begin{bmatrix} 0 & 0 & 0 & \dots & 0 & -q_0 \\ 1 & 0 & 0 & \dots & 0 & -q_1 \\ 0 & 1 & 0 & \dots & 0 & -q_2 \\ \vdots & \vdots & \vdots & \ddots & \vdots & \vdots \\ 0 & 0 & 0 & \dots & 0 & -q_{n-2} \\ 0 & 0 & 0 & \dots & 1 & -q_{n-1} \end{bmatrix}, \mathbf{E}_c^{(H)} = \begin{bmatrix} p_0 \\ p_1 \\ p_2 \\ p_3 \\ \vdots \\ p_{n-1} \end{bmatrix}, \mathbf{Q}_c^{(H)} = \begin{bmatrix} 0 \\ 0 \\ 0 \\ 0 \\ \vdots \\ 1 \end{bmatrix}^T$$

\mathbf{X} , $\mathbf{D}_c^{(H)}$, $\mathbf{E}_c^{(H)}$ and $\mathbf{Q}_c^{(H)}$ are different among each of the 36 state space models and can be determined by curve fitting the expression presented in Eq. (7) to the transfer functions defined by added mass and damping coefficients. Considering all degrees of freedom and the frequency-independent term, the radiation forces can be written as

$$\begin{cases} \mathbf{F}_{Rad} = \mathbf{M}_h(\infty) \ddot{\mathbf{u}}(t) + \mathbf{z}_{Rad}(t) \\ \mathbf{z}_{Rad}(t) = [z_1^{(Rad)}(t) z_2^{(Rad)}(t) \dots z_6^{(Rad)}(t)]^T \\ z_i^{(Rad)}(t) = \sum_{j=1}^6 z_{ij}^{(Rad)}(t) \\ \dot{\mathbf{X}}(t) = \mathbf{D}_c^{(H)} \mathbf{X}(t) + \mathbf{E}_c^{(H)} \dot{u}_j(t) \\ z_{ij}^{(Rad)}(t) = \mathbf{Q}_c^{(H)} \mathbf{X}(t) \end{cases} \quad (9)$$

2.1.2. Aerodynamic self-excited forces

Similar to the radiation forces, the aerodynamic self-excited forces $\mathbf{q} = [q_y \ q_z \ q_\theta]^T$ can be expressed as follows:

$$\mathbf{q} = \mathbf{C}_{ae}(K) \dot{\mathbf{u}} + \mathbf{K}_{ae}(K) \mathbf{u} \quad (10)$$

The positive direction of the displacement \mathbf{u} and the forces \mathbf{q} are displayed in Fig. 3. The aerodynamic damping matrix $\mathbf{C}_{ae}(K)$, and the aerodynamic stiffness matrix, $\mathbf{K}_{ae}(K)$, contain 18 aerodynamic derivatives, P_n^* , H_n^* and A_n^* , $n \in \{1, 2, \dots, 6\}$, which are cross-sectional properties that are functions of the reduced frequency of motion $K = (B\omega)/V$.

$$\mathbf{C}_{ae} = \frac{1}{2} \rho V K B \begin{bmatrix} P_1^* & P_5^* & B P_2^* \\ H_5^* & H_1^* & B H_2^* \\ B A_5^* & B A_1^* & B^2 A_2^* \end{bmatrix}, \mathbf{K}_{ae} = \frac{1}{2} \rho V^2 K^2 \begin{bmatrix} P_4^* & P_6^* & B P_3^* \\ H_6^* & H_4^* & B H_3^* \\ B A_6^* & B A_4^* & B^2 A_3^* \end{bmatrix}$$

Here, V represents the mean wind velocity, ρ is the air density, B is the width of the girder, and ω refers to the oscillation frequency of the bridge deck. The aerodynamic derivatives are commonly determined by wind tunnel tests [25]. Eq. (10) is only valid for a single-frequency harmonic motion, but the model can be extended to any periodic or aperiodic motion through Fourier integral representation:

$$\mathbf{G}_q(\omega) = (i\omega \mathbf{C}_{ae}(\omega) + \mathbf{K}_{ae}(\omega)) \mathbf{G}_u(\omega) = \mathbf{F}(\omega) \mathbf{G}_u(\omega) \quad (11)$$

Here, $\mathbf{G}_q(\omega)$ and $\mathbf{G}_u(\omega)$ are the Fourier transforms of self-excited forces and displacements, respectively. By applying the inverse

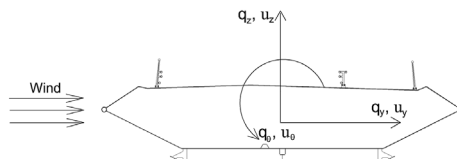


Fig. 3. Aerodynamic forces acting on the bridge section considered in this study.

Fourier transform to Eq. (11), the self-excited forces in the time domain can be expressed as a convolution integral as follows:

$$\mathbf{q}(t) = \int_{-\infty}^{\infty} \mathbf{f}(t - \tau) \mathbf{u}(\tau) d\tau$$

Here, $\mathbf{f}(t)$ and $\mathbf{u}(t)$ are the inverse Fourier transforms of $\mathbf{F}(\omega)$ and $\mathbf{G}_u(\omega)$, respectively. The aerodynamic derivatives are only available at discrete reduced frequencies. A rational function [13–15,26], as expressed in Eq. (12), is widely used to curve fit the scattered experimental data of aerodynamic derivatives and calculate the integration in the equation above.

$$\mathbf{F}(\omega) = \frac{1}{2} \rho V^2 \left(\mathbf{a}_1 + \mathbf{a}_2 \frac{i\omega B}{V} + \sum_{l=1}^{N-3} \mathbf{a}_{l+3} \frac{i\omega B/V}{i\omega B/V + d_l} \right) \quad (12)$$

The unknowns \mathbf{a}_1 , \mathbf{a}_2 , \mathbf{a}_{l+3} and d_l in the rational function can be obtained by a least squares fit to the experimental data of the aerodynamic derivatives.

Similar to modeling radiation forces, the transfer function presented above can be expressed as a state space model. Integration of the distributed self-excited forces by applying the principle of virtual work and introducing the state space model yields the following expression for the nodal forces [15,27]:

$$\begin{cases} \mathbf{F}_{se} = \mathbf{A}_1 \mathbf{u}(t) + \mathbf{A}_2 \dot{\mathbf{u}}(t) + \mathbf{z}_{se}(t) \\ \dot{\mathbf{X}}(t) = \mathbf{D}_c^{(ae)} \mathbf{X}(t) + \mathbf{E}_c^{(ae)} \dot{\mathbf{u}}(t) \\ \mathbf{z}_{se}(t) = \mathbf{Q}_c^{(ae)} \mathbf{X}(t) \end{cases} \quad (13)$$

where

$$\begin{aligned} \mathbf{A}_1 &= \frac{1}{2} \rho V^2 \int_0^L \mathbf{N}^T(\mathbf{y}) \mathbf{a}_1 \mathbf{N}(\mathbf{y}) d\mathbf{y}; \quad \mathbf{A}_2 = \frac{1}{2} \rho V^2 \frac{B}{V} \int_0^L \mathbf{N}^T(\mathbf{y}) \mathbf{a}_2 \mathbf{N}(\mathbf{y}) d\mathbf{y}; \\ \mathbf{D}_c^{(ae)} &= \frac{V}{B} \begin{bmatrix} d_1 \mathbf{I} & & & \\ & d_1 \mathbf{I} & & \\ & & \ddots & \\ & & & d_{N-3} \mathbf{I} \end{bmatrix}; \quad \mathbf{E}_c^{(ae)} = [\mathbf{I} \quad \mathbf{I} \quad \cdots \quad \mathbf{I}]^T; \\ & \quad \mathbf{Q}_c^{(ae)} = [\mathbf{A}_4 \quad \mathbf{A}_5 \quad \cdots \quad \mathbf{A}_N]; \quad \mathbf{X} = [\mathbf{x}_1 \quad \mathbf{x}_2 \quad \cdots \quad \mathbf{x}_{N-3}]^T \end{aligned}$$

Here, $\mathbf{A}_{l+3} = \frac{1}{2} \rho V^2 \int_0^L \mathbf{N}^T(\mathbf{y}) \mathbf{a}_{l+3} \mathbf{N}(\mathbf{y}) d\mathbf{y}$ and $\mathbf{x}_l = \mathbf{u}(t) - \frac{d_l V}{B} \int_{-\infty}^t e^{-(d_l V/B)(t-\tau)} \mathbf{u}(\tau) d\tau$. The matrix $\mathbf{N}(\mathbf{y})$ includes the shape functions, and L refers to the length of the beam element.

2.1.3. Implementation in ABAQUS

The equation of motion for the combined structure and flow system is obtained when Eqs. (9) and (13) are introduced into Eq. (1):

$$\begin{cases} (\mathbf{M}_s + \mathbf{M}_h(\infty)) \ddot{\mathbf{u}}(t) + (\mathbf{C}_s - \mathbf{A}_2) \dot{\mathbf{u}}(t) + (\mathbf{K}_s + \mathbf{K}_h - \mathbf{A}_1) \mathbf{u}(t) - \mathbf{z}_{se}(t) + \mathbf{z}_{Rad}(t) = \mathbf{F}_{Mean} + \mathbf{F}_{Buff}(t) + \mathbf{F}_{WA}^{(1)}(t) + \mathbf{F}_{WA}^{(2\pm)}(t) \\ \text{Aerodynamic part } \mathbf{z}_{se}(t): \\ \dot{\mathbf{X}}(t) = \mathbf{D}_c^{(ae)} \mathbf{X}(t) + \mathbf{E}_c^{(ae)} \dot{\mathbf{u}}(t) \\ \mathbf{z}_{se}^{(se)}(t) = \mathbf{Q}_c^{(ae)} \mathbf{X}(t) \\ \text{Hydrodynamic part } \mathbf{z}_{Rad}(t): \\ \mathbf{z}_{Rad}(t) = [\mathbf{z}_1^{(Rad)}(t) \quad \mathbf{z}_2^{(Rad)}(t) \quad \cdots \quad \mathbf{z}_6^{(Rad)}(t)]^T \\ \mathbf{z}_i^{(Rad)}(t) = \sum_{j=1}^6 \mathbf{z}_{ij}^{(Rad)}(t) \\ \dot{\mathbf{X}}(t) = \mathbf{D}_c^{(H)} \mathbf{X}(t) + \mathbf{E}_c^{(H)} \dot{\mathbf{u}}_j(t) \\ \mathbf{z}_{ij}^{(Rad)}(t) = \mathbf{Q}_c^{(H)} \mathbf{X}(t) \end{cases} \quad (14)$$

The motion-induced hydrodynamic and aerodynamic forces are modeled using similar state space models.

$$\begin{cases} \dot{\mathbf{X}}(t) = \mathbf{D}_c \mathbf{X}(t) + \mathbf{E}_c \dot{\mathbf{u}}(t) \\ \mathbf{z}(t) = \mathbf{Q}_c \mathbf{X}(t) \end{cases} \quad (15)$$

As shown above, the velocity of the structure is the input of the model, whereas a vector of the motion-induced forces is the output of the model. \mathbf{X} represents the aerodynamic or hydrodynamic state variables. These variables must be included when solving the equation of motion for the combined structure and flow system. The starting point is to transform the continuous first-order linear inhomogeneous differential equation presented in Eq. (15) to a discrete form [28].

$$\begin{cases} \mathbf{X}_{k+1} = \mathbf{D} \mathbf{X}_k + \mathbf{E} \dot{\mathbf{u}}_k + \mathbf{G}[(1 - \gamma) \ddot{\mathbf{u}}_k + \gamma \ddot{\mathbf{u}}_{k+1}] \\ \mathbf{z}_k = \mathbf{Q} \mathbf{X}_k \end{cases} \quad (16)$$

here, $\mathbf{D} = e^{\mathbf{D}_c \Delta t}$, $\mathbf{E} = (\mathbf{D} - \mathbf{I}) \mathbf{D}_c^{-1} \mathbf{E}_c$, $\mathbf{G} = \mathbf{D}_c^{-1} (\mathbf{E} - \mathbf{E}_c \Delta t)$ and $\mathbf{Q} = \mathbf{Q}_c$.

Algorithm 1 illustrates how the state variables are updated at each time step in the dynamic analysis by defining a user element. The elements are modeled on top of the nodes of ordinary beam elements such that it is not necessary to involve the mass, damping and stiffness terms related to the structure. A first-order hold assumption is introduced for the discretization of velocity; otherwise, \mathbf{G}

will be zero. Under the first-order hold assumption, a much larger time step is allowed in the numerical integration of the equation of motion than can be used based on the zero-order hold assumption [27]. However, the assumption makes the state-space model more complicated because the state variables are dependent on acceleration in the current time step. Therefore, it is necessary to re-organize Eq. (16) and introduce a new variable $\tilde{\mathbf{X}}_k = \mathbf{D}\mathbf{X}_{k-1} + \mathbf{E}\dot{\mathbf{u}}_{k-1} + \mathbf{G}(1 - \gamma)\ddot{\mathbf{u}}_{k-1}$ such that $\tilde{\mathbf{X}}_k$ depends only on the motion in the previous time step and the term $\mathbf{G}\gamma\ddot{\mathbf{u}}_k$ can be added directly into the mass matrix of the system. $\mathbf{M}_h(\infty)$, \mathbf{A}_2 and \mathbf{A}_1 are constant matrices and can be conveniently modeled by defining them as the mass, damping and stiffness of the user element, respectively.

Algorithm 1. Simulation of the self-excited force by the user element in ABAQUS.

Step (1): ABAQUS supplies current estimates of \mathbf{u}_k , $\dot{\mathbf{u}}_k$ and $\ddot{\mathbf{u}}_k$

Step (2): Load $\tilde{\mathbf{X}}_{k-1}$, $\dot{\mathbf{u}}_{k-1}$ and $\ddot{\mathbf{u}}_{k-1}$ from the last time step (the initial value of $\tilde{\mathbf{X}} : \tilde{\mathbf{X}}_0 = \mathbf{0}$) and calculate the state vector \mathbf{X}_{k-1}

$$\mathbf{X}_{k-1} = \tilde{\mathbf{X}}_{k-1} + \mathbf{G}\gamma\ddot{\mathbf{u}}_{k-1}$$

Step (3): Calculate the residual force and Jacobian matrix

$$\mathbf{R}_k = \mathbf{M}_{user}\ddot{\mathbf{u}}_k + \mathbf{C}_{user}\dot{\mathbf{u}}_k + \mathbf{K}_{user}\mathbf{u}_k + \mathbf{Q}\tilde{\mathbf{X}}_k$$

$$\mathbf{J} = \mathbf{M}_{user}\frac{1}{\beta\Delta t^2} + \mathbf{C}_{user}\frac{\gamma}{\beta\Delta t} + \mathbf{K}_{user}$$

where \mathbf{M}_{user} , \mathbf{C}_{user} , and \mathbf{K}_{user} are the mass, damping and stiffness, respectively, of the user element:

$$\mathbf{M}_{user} = -\mathbf{Q}\mathbf{G}\gamma, \mathbf{C}_{user} = -\mathbf{A}_2, \mathbf{K}_{user} = -\mathbf{A}_1 \quad \text{for the aerodynamic user element}$$

$$\mathbf{M}_{user} = \mathbf{M}_h(\infty) - \mathbf{Q}\mathbf{G}\gamma, \mathbf{C}_{user} = 0, \mathbf{K}_{user} = 0 \quad \text{for the hydrodynamic user element}$$

$\tilde{\mathbf{X}}_k$ depends only on the motion in step $k-1$:

$$\tilde{\mathbf{X}}_k = \mathbf{D}\mathbf{X}_{k-1} + \mathbf{E}\dot{\mathbf{u}}_{k-1} + \mathbf{G}(1 - \gamma)\ddot{\mathbf{u}}_{k-1}$$

β and γ are the two parameters in Newmark's method

Step (4): ABAQUS calculates new values for \mathbf{u}_k , $\dot{\mathbf{u}}_k$ and $\ddot{\mathbf{u}}_k$ and performs equilibrium iterations until the results converge.

Step (5): Save $\tilde{\mathbf{X}}_k$, $\dot{\mathbf{u}}_k$ and $\ddot{\mathbf{u}}_k$ in ABAQUS as solution-dependent variables

Step (6): Return to (1) for new time step or stop

2.2. Buffeting forces

2.2.1. Simulation of the wind velocities

The wind field is simulated using Monte Carlo analysis [29,30]. The density of the air is assumed to be $\rho = 1.25 \text{ kg/m}^3$, and the cross-spectral densities of the horizontal along-wind velocity u and vertical components w at points i and j are assumed to be given as follows:

$$S_{uu}(\omega, \Delta x, \Delta z, z) = \sqrt{\frac{40.58V_i z_i \kappa}{(1 + 9.74\omega z_i / V_i)^{5/3}}} \sqrt{\frac{40.58V_j z_j \kappa}{(1 + 9.74\omega z_j / V_j)^{5/3}}} \exp\left(-\frac{3.18\omega \sqrt{(\Delta x)^2 + (\Delta z)^2}}{V_i + V_j}\right)$$

$$S_{ww}^+(\omega, \Delta x) = \frac{0.82V\kappa}{(1 + 0.79\omega z / V)^{5/3}} \exp\left(-\frac{\Delta x\omega}{V}\right)$$

$$S_{uw}^+(\omega, \Delta x) = \frac{2.23V\kappa}{(1 + 1.67\omega z / V)^{7/3}} \exp\left(-\frac{\Delta x\omega}{V}\right) \quad (17)$$

where κ is the roughness coefficient at the site, which is assumed to be 0.0031; z_i and z_j are the heights above the ground at the two points; and Δx and Δz are the lateral and vertical distances, respectively, between the two points considered.

The vertical curvature of the girder is neglected by using the height at the middle of the bridge as the reference for the wind load of the girder. It is further assumed that only the along-wind turbulence component u provides wind loading on the pylons and that the vertical mean wind velocity profile is given by

$$\frac{V(h)}{V_{ref}} = \left(\frac{h}{h_{ref}}\right)^\alpha \quad (18)$$

Here, V_{ref} and $V(h)$ are the mean wind velocity at the reference point and at height h , respectively, and α is related to the surface roughness. The wind velocities on the girder and pylons are simulated independently, neglecting a possible correlation. This assumption is an approximation in the areas near the connection between the pylons and girder.

2.2.2. Linear and nonlinear wind forces

The mean and buffeting forces due to the mean and turbulent wind are calculated using quasi-steady theory [31] when the

aerodynamic admittance is neglected. Assuming that the fluctuating flow components, $u(x, t)$ and $w(x, t)$, and the structural velocity are small compared to the mean wind velocity V , the linearized wind-induced forces can be defined as

$$\mathbf{F}_{mean} + \mathbf{F}_{Buff}(t) = \frac{\rho V^2 B}{2} \begin{bmatrix} (D/B)\bar{C}_D \\ \bar{C}_L \\ B\bar{C}_M \end{bmatrix} + \frac{\rho VB}{2} \begin{bmatrix} 2(D/B)\bar{C}_D(D/B)C'_D - C'_L \\ 2\bar{C}_L & C'_L + (D/B)\bar{C}_D \\ 2B\bar{C}_M & BC'_M \end{bmatrix} \begin{bmatrix} u(x, t) \\ w(x, t) \end{bmatrix} \quad (19)$$

here, D is the height of the girder. \bar{C}_D , \bar{C}_L and \bar{C}_M are the mean values of the drag, lift and torsional moment force coefficients, respectively, and C'_D , C'_L and C'_M are their derivatives with respect to the angle of attack.

At the peaks of the turbulent wind velocities, the higher-order terms can significantly contribute to the wind loading and can thus significantly contribute to the load effects in certain situations. The buffeting forces are modeled using the following expression to investigate the influence of the nonlinear terms.

$$\mathbf{F}_{mean} + \mathbf{F}_{Buff}(t) = \frac{1}{2}\rho V_{rel}^2 \begin{bmatrix} \cos \beta & -\sin \beta & 0 \\ \sin \beta & \cos \beta & 0 \\ 0 & 0 & 1 \end{bmatrix} \begin{bmatrix} D(\bar{C}_D + \beta C'_D) \\ B(\bar{C}_L + \beta C'_L) \\ B^2(\bar{C}_M + \beta C'_M) \end{bmatrix}$$

$$V_{rel}^2 = (V + u(x, t))^2 + w(x, t)^2$$

$$\beta \approx \arctan\left(\frac{w(x, t)}{V + u(x, t)}\right) \quad (20)$$

2.3. Wave excitation forces

The hydrodynamic actions consist of hydrostatic forces, radiation forces and wave excitation forces [32]. The hydrostatic forces are frequency independent and modeled as springs in the finite element model of the structure, whereas the radiation forces are modeled using state space models, as presented in chapter 2.1. The wave excitation forces related to the fluctuating pressure on the submerged surface of the pylons are caused by incident waves assuming that the structure is fixed. As noted above, the fluid-structure interaction effects are commonly modeled using potential theory; in this paper, we will consider second-order difference and sum frequency forces as well as first-order forces. Higher-order models exist but are outside the scope of this paper.

2.3.1. First-order wave excitation forces

The first-order forces are always larger than the second-order forces and are defined by a transfer function that can be obtained by potential theory. The amplitude of the first-order wave forces is proportional to the wave amplitude. In irregular waves, the first-order forces can be obtained by summing the contributions from all of the frequency components and directions using the following well-known expression [33]:

$$\mathbf{F}_{WA}^{(1)}(x, y, t) = \sum_n^N \sum_m^M |\mathbf{T}^{(1)}(\omega_n, \theta_m)| \eta_{nm} \cos[k_n(x \cos(\theta_m) + y \sin(\theta_m)) - \omega_n t + \varepsilon_{mn} - \phi_{mn}], i \in \{1, 2, \dots, 6\}$$

$$\eta_{nm} = \sqrt{2S_\eta(\omega_n, \theta_m)\Delta\omega\Delta\theta}$$

$$\phi_{mn} = \tan^{-1}\left(\frac{\text{Im}(\mathbf{T}^{(1)}(\omega_n, \theta_m))}{\text{Re}(\mathbf{T}^{(1)}(\omega_n, \theta_m))}\right) \quad (21)$$

here, $\mathbf{T}^{(1)}(\omega, \theta)$ is the first-order transfer function and represents the force generated by a unit amplitude regular wave with frequency ω propagating from the direction θ . The wave amplitude and wave number are denoted by η and k , respectively; for small-amplitude waves, the wave number is related to the frequency and water depth h by the dispersion relation, $\omega^2 = gk \tanh(kh)$. $\varepsilon_{mn} \in \{0 \dots 2\pi\}$ is a uniformly distributed random phase angle. $S_\eta(\omega, \theta)$ represents the wave spectrum and is a function of both the wave frequency and direction.

$$S_\eta(\omega, \theta) = S(\omega)D(\omega, \theta) \quad (22)$$

here, $S(\omega)$ is the unidirectional wave spectral density and $D(\omega, \theta)$ is the directional distribution. The directional distribution for locally wind-generated sea is commonly approximated as frequency independent. Little information regarding the wave conditions at the site is currently available, making the one parameter Pierson-Moskowitz spectrum [34] a tempting choice. Meanwhile, cos-2s distribution [35] is applied to represent the wave direction distribution in this study.

$$S(\omega) = 0.0081g^2\omega^{-5} \exp\left(-\frac{3.11}{\omega^4 H_s^2}\right)$$

$$D(\theta) = \frac{\Gamma(s+1)}{2\sqrt{\pi}\Gamma(s+1/2)} \cos^{2s}\left(\frac{\theta}{2}\right) \quad (23)$$

where H_s is significant wave height and s is a parameter which determines the concentration of the direction distribution of the wave energy.

2.3.2. Difference frequency forces

The natural frequencies of the low-order modes of the bridge are well below the energy content in the wave spectra such that

these modes will not be excited by first-order excitation forces. However, the difference frequency forces can cause wave excitations in this frequency range. For short-crested waves, the different frequency forces can be written as follows [36–38]:

$$\mathbf{F}_{WA}^{(2-)} = \text{Re} \sum_{l=1}^N \sum_{h=1}^N \sum_{j=1}^N \sum_{k=1}^N \eta_{jl} \eta_{kh} \mathbf{T}^{(2-)}(\omega_j, \omega_k, \theta_l, \theta_h) e^{i(\omega_k - \omega_j)t} e^{i(\varepsilon_{kh} - \varepsilon_{jl})} \quad (24)$$

where $\mathbf{T}^{(2-)}$ contains the in-phase and out-of-phase components of the full quadratic transfer function, \mathbf{T}^{ic} and \mathbf{T}^{is} , respectively, and represents the forces induced by the interaction of a unit-amplitude wave associated with frequency ω_j and direction θ_l and a unit-amplitude wave associated with frequency ω_k and direction θ_h . The direction interaction effects are ignored in the case study, i.e., the terms where $\theta_l \neq \theta_h$. Thus, the difference frequency forces can be written as

$$\mathbf{F}_{WA}^{(2-)} = \text{Re} \sum_{l=1}^N \sum_{j=1}^N \sum_{k=1}^N \eta_{jl} \eta_{kl} \mathbf{T}^{(2-)}(\omega_j, \omega_k, \theta_l) e^{i(\omega_k - \omega_j)t} e^{i(\varepsilon_{kl} - \varepsilon_{jl})} \quad (25)$$

This will reduce the computational effort significantly, as fewer quadratic transfer functions are required. The mean drift force is included in the equation above and can be found by setting $\omega_k = \omega_j$:

$$\bar{\mathbf{F}}_{WA} = \sum_{l=1}^N \sum_{j=1}^N 2S_{\eta}(\omega_j, \theta_l) \mathbf{T}^{ic}(\omega_j, \omega_j, \theta_l) \Delta\omega \Delta\theta \quad (26)$$

2.3.3. Sum frequency forces

The sum frequency forces introduce excitation at higher frequencies compared to the first-order excitation forces and may be important for the heave, pitch and roll motions of the pylons. If the directional interactions are ignored, the time series of summed frequency forces can be written as follows [38].

$$\mathbf{F}_{WA}^{(2+)} = \text{Re} \sum_{l=1}^N \sum_{j=1}^N \sum_{k=1}^N \eta_{jl} \eta_{kl} \mathbf{T}^{(2+)}(\omega_j, \omega_k, \theta_l) e^{i(\omega_k + \omega_j)t} e^{i(\varepsilon_{kl} + \varepsilon_{jl})} \quad (27)$$

3. Numerical simulations

A comprehensive finite element model of the bridge, as displayed in Fig. 4, is used in the dynamic analysis. Each of the main girder spans has a length of 1385 m and the pylons are 198 m high and have a draft of 65 m. The bending stiffness of the girder for horizontal, vertical and torsional deflections are $3.22 \cdot 10^{12} \text{Nm}^2$, $2.04 \cdot 10^{11} \text{Nm}^2$, and $1.99 \cdot 10^{11} \text{Nm}^2$ respectively. The main cable and hanger have a cross section area of 0.333 and 0.032m^2 , respectively. More details about the finite element model of the bridge are presented in Ref. [39]. The girder, main cable, tethers, hangers and pylons are modeled by beam elements. The aerodynamic self-excited and hydrodynamic radiation forces are simulated by implementing a user element in ABAQUS. The user element is developed as a one-node element and is included in the nodes of the girder and a reference point on each of the floating pylons; the user elements are illustrated by the red markers in Fig. 4. The added mass, potential damping and first- and second-order transfer functions for the wave excitation forces are obtained using potential theory. Fig. 5 shows the hydrodynamic panel model of the submerged part of the pylon and the free water surface. The panel model of the free water surface is only required when calculating the full quadratic transfer functions based on the near-field formulation [37]. The side span on the right hand side of the Artist's view in Fig. 1 has not been included in the modeling.

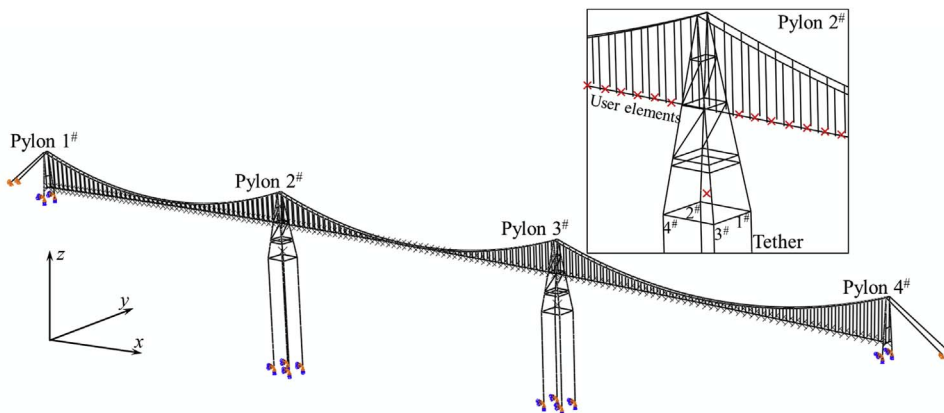


Fig. 4. Finite element model of the three-span suspension bridge with two floating pylons.

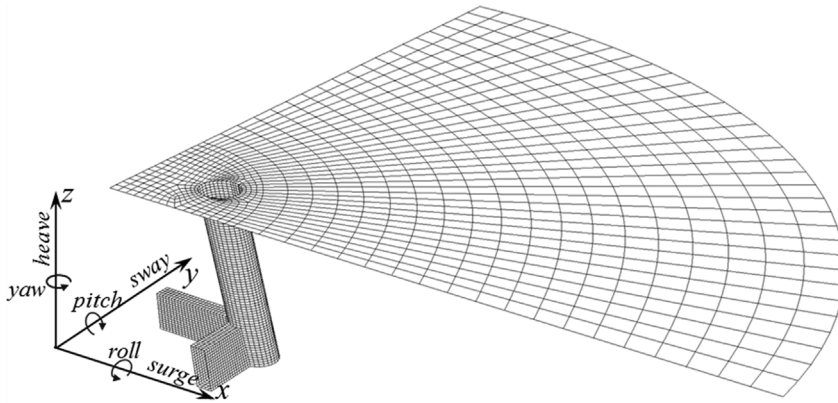


Fig. 5. One quarter of the panel model of the submerged part of the pylon and the water surface in WADAM.

3.1. Estimation of the parameters in the state space models

3.1.1. Potential added mass and damping

The potential added mass and damping at discrete frequencies are obtained by linear potential theory using the software WADAM [40]. The numerical results for selected components of the added mass and potential damping are displayed in Fig. 6. The rational function presented in Eq. (6) is used to curve fit the data. The unknowns $\theta = [p_{n-1}, \dots, p_0, q_{n-1}, \dots, q_0]^T$ can be obtained by regression in the frequency domain:

$$\theta = \arg \min \sum_l \frac{|\dot{U}_j(i\omega_l, \theta)H(\omega_l) - Z_{ij}^{(H)}(i\omega_l, \theta)|^2}{|\dot{U}_j(i\omega_l, \theta)|^2} \quad (28)$$

This method has been implemented in a MATLAB toolbox, *FDI_Toolbox_v1.2*, by Perez and Fossen [41], which is applied in this study. A high-order polynomial of the transfer functions must be applied, as there are many fluctuations in the numerical results for the added mass and damping. Fig. 6 shows that the models fit the data well.

3.1.2. Aerodynamic derivatives

The self-excited forces are modeled by fitting rational functions to the transfer function defined in terms of the aerodynamic derivatives. The accuracy of the numerical simulations depends on the quality of the curve fit of the expressions presented in Eq. (12) to the experimental data of the aerodynamic derivatives. The self-excited forces must be captured precisely throughout the reduced frequency range, particularly in the range corresponding to the natural frequencies of the system. Experimental aerodynamic derivative data [42] from forced vibrations tests of the cross section of Hardanger Bridge are represented by circles and triangles in Fig. 7, and the solid lines are curve fits defined by the rational functions introduced in Eq. (12). As shown in Fig. 7, the curve fits match well

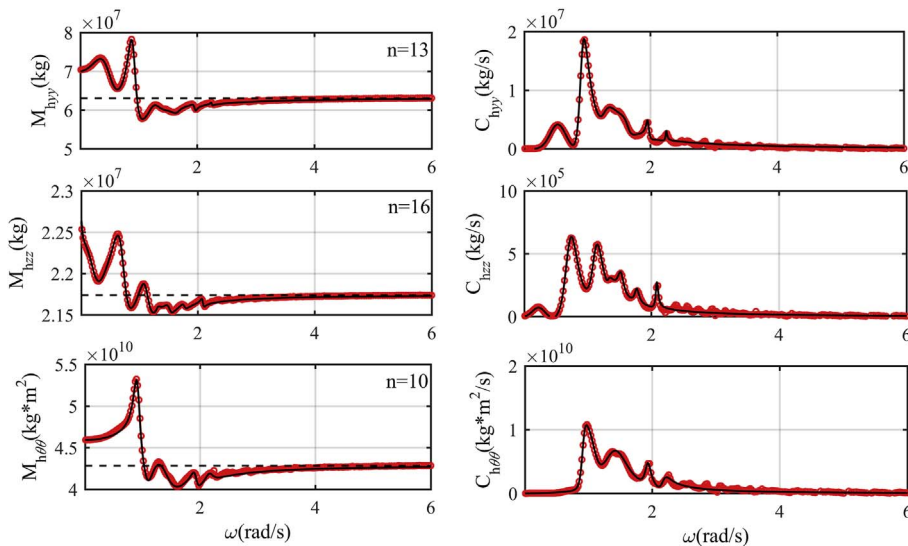


Fig. 6. Selected added mass and damping coefficients. The order of the transfer functions n is given in the figures.

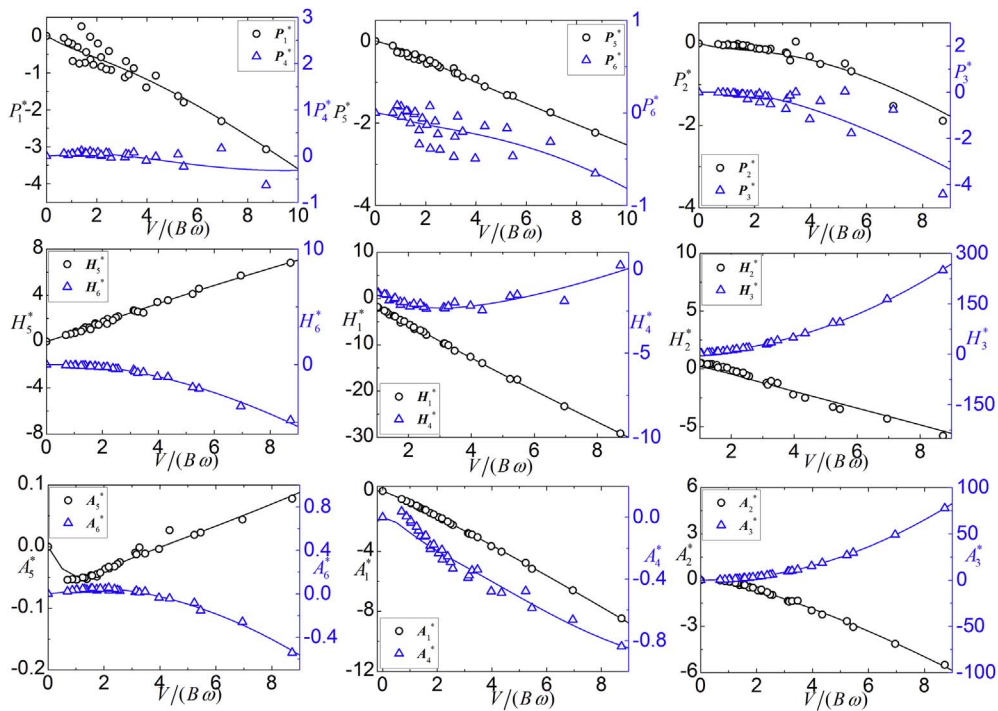


Fig. 7. Curve fits of the 18 aerodynamic derivatives obtained by forced vibration tests.

with the experimental data. We have applied the shape of the girder of the Hardanger Bridge in this study since wind tunnel tests are available for this section.

3.2. Simulation of the wind and wave loads

Eqs. (17–27) are used to generate the wind and wave forces acting on the pylons and girder. The surface roughness related parameter α in Eq. (18), assumed to be 0.12, is according to [43] due to the lack of specific data at Bjørnafjorden. The fluctuating wind velocities have been simulated at 151 points along the girder and 40 points along the pylons, with cut-off frequencies of $\omega_u = 60$ rad/s and $\Delta\omega = 0.001$ rad/s, respectively. Rather small difference of the response statistics is observed when applying more points along the girder, which infers that 151 points can represent the wind field very well. The following force coefficients of the girder were obtained from wind tunnel experiments [44]: $\bar{C}_D = 0.70$, $C'_D = 0$, $\bar{C}_L = -0.25$, $C'_L = 2.4$, $\bar{C}_M = 0.01$ and $C'_M = 0.74$. The wave amplitude of the first- and second-order wave excitation force transfer functions, $\mathbf{T}_{\text{wave}}^{(1)}$ and $\mathbf{T}_{\text{wave}}^{(2\pm)}$, are calculated by WADAM. The time series of the buffeting wind force and the first- and second-order wave excitation forces in the y-direction are shown in Fig. 8; here, a mean wind velocity of 35 m/s and significant wave height of 4.88 m are applied. The average estimated spectral density of 10 realizations is compared to the target spectral density in Fig. 9 to verify that the time domain simulations correspond to the target spectral densities.

The magnitude of the wind force and second-order difference force is very small compared to the others, but they are dominant in the frequency range of 0–0.3 rad/s. The natural frequencies of the first ten modes and first three torsional modes considering the mean wind force at $V = 35$ m/s and the added mass as the frequency goes to infinity are listed in Table 1. The first three natural modes of the structure have frequencies in this range, making the forces important for the dynamic behavior of the system. The first-order wave excitation forces are dominant in the frequency range of 0.3–1.2 rad/s, which may excite several higher modes of the girder. The second-order sum force is in the range of 1.7–3 rad/s, which can be important for modes where the pylons move in heave, pitch and roll.

3.3. Computational efficiency and validation

The time domain methodology outlined in this paper should provide the same response as a multimode frequency domain analysis if the system is linear and a sufficient number of modes are included in the model. The time domain simulations should be verified by comparing the response statistics with results from a frequency domain analysis. Multimode theory is briefly introduced in the Appendix.

The wind-induced dynamic responses of the floating suspension bridge are calculated using the time and frequency domain approaches; here, a mean wind velocity of 35 m/s and significant wave height of 4.88 m are implemented. Turbulent wind forces acting on the pylon and nonlinear effects are not considered in the validation step. The standard deviation of the displacement along

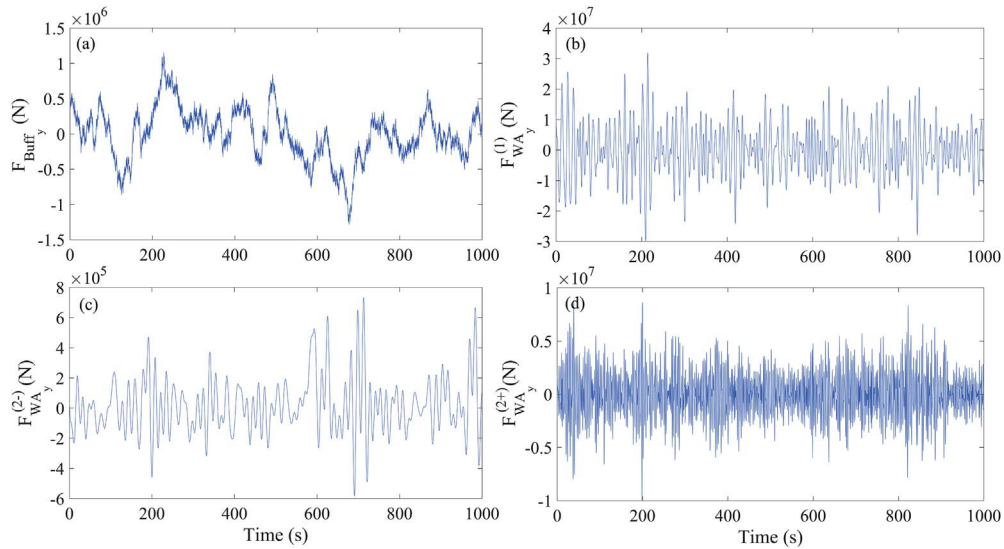


Fig. 8. (a) Wind force in the y-direction over one span length (1385 m). (b), (c) and (d) show the first-order, second-order difference and sum frequency wave excitation forces in the y-direction on one floating pylon, respectively.

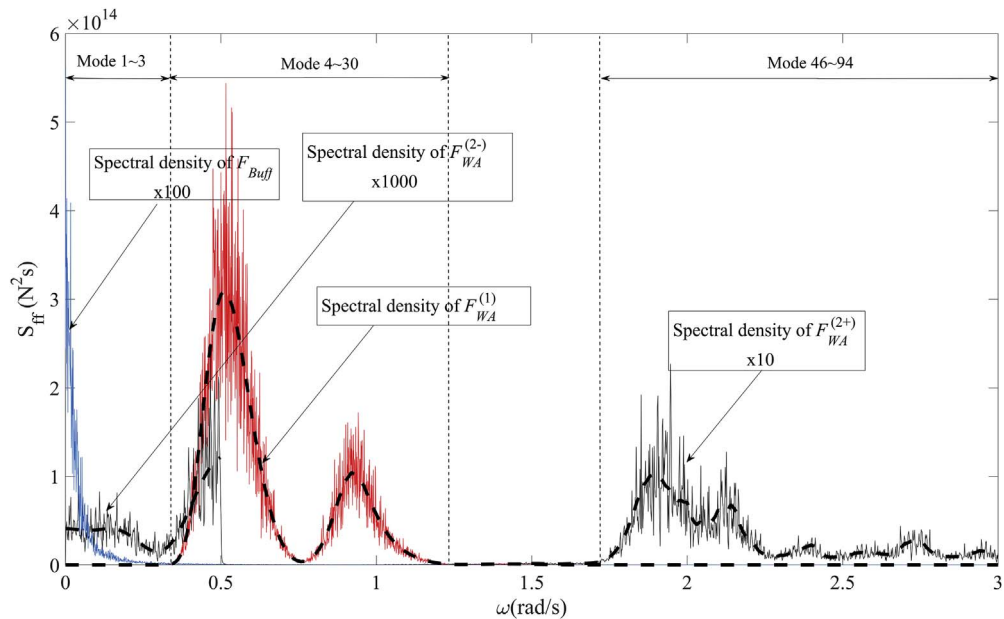


Fig. 9. Auto spectral density of the wind and wave forces presented in Fig. 8. Dashed lines are the target spectral densities, whereas each solid line represents the average spectral density for 10 realizations.

the girder for five 1-h time domain simulations is compared to the frequency domain results in Fig. 10. The responses in the y-direction in the time domain simulations are scattered due to the large first natural period. A longer time domain simulation may be more appropriate in this analysis. However, there is still good agreement between the mean response values along the entire girder.

The variance of the pylon displacement obtained from the time series is compared to the frequency domain results in Table 2. The discrepancy is large for several cases, such as cases 1 and 5 for the sway response and case 1 for the heave motion. However, the mean values correspond well. Thus, the time domain simulations capture the dynamic behavior accurately.

In addition to the accuracy, computation efficiency is another important criterion to evaluate a new numerical methodology. To test the efficiency of the presented time domain methodology, we compared the computational time with and without the user elements in ABAQUS. The frequency dependency of the motion induced hydrodynamic and aerodynamic forces are thus neglected when the user elements are not applied. The finite element model consists of 1311 beam elements, 300 user elements to simulate the aerodynamic self-excited forces and 20 user elements for radiation force. Simulations were run on a computer with 2.6 GHz CPU. The average computational time required is 8.01 and 7.08 h, respectively. Including the user elements only require 13% more

Table 1

Natural frequency for the first ten modes and the first three torsional modes. H, V and T refer to horizontal, vertical and torsional vibration modes, respectively.

Mode no.	Natural frequency (rad/s)	Type
1	0.0724	H
2	0.0968	H
3	0.186	V
4	0.307	H
5	0.317	H
6	0.359	H
7	0.464	H
8	0.518	H&V
9	0.563	V
10	0.643	H
51	1.845	T
52	1.868	T
54	2.001	T

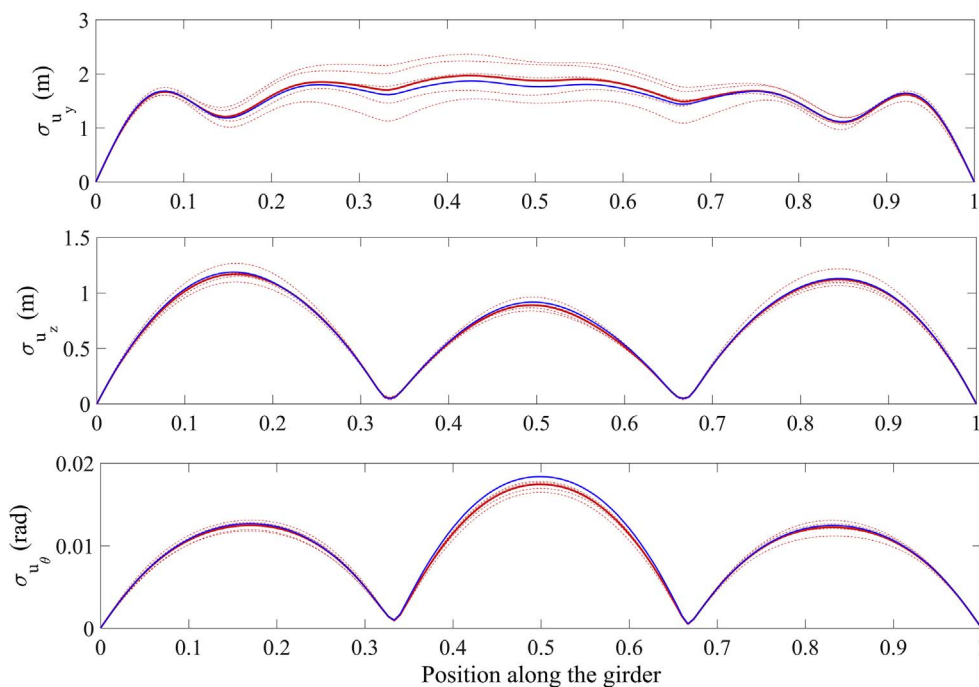


Fig. 10. Standard deviations of the displacement along the girder in the lateral, vertical and torsional directions. (a) lateral displacement, (b) vertical displacement, (c) torsional displacement. The red dashed line --- represents the standard deviation of each realization, the solid red line — is the average of the 5 realizations, and the solid blue line — is the frequency domain results. (For interpretation of the references to color in this figure legend, the reader is referred to the Web version of this article.)

computational time when simulating the frequency-dependent forces based on the presented time domain methodology.

3.4. Nonlinear effects

Geometric nonlinearity and nonlinear buffeting forces are considered in the numerical simulation of the suspension bridge subjected to mean and turbulent wind forces, and first- and second-order wave excitation forces. The results are compared to the linear analysis results to study the nonlinear effects on the section forces in the girder and tethers.

The results are presented in Table 3. For the tethers, geometric nonlinearities and nonlinear buffeting forces make very few differences in the standard deviation of the tension force compared to the linear case, respectively. Nonlinear effects appear to be insignificant for these components of the bridge. Fig. 11 shows the section moment along the girder for the linearized and nonlinear systems. Geometric nonlinearities have a minor influence, whereas the nonlinear buffeting forces result in higher standard deviations for vertical bending and torsional moment at the middle of each span, respectively. However, the difference due to nonlinear buffeting forces is smaller for the highest section moment on the girder near the pylons.

Table 2

Comparison of the time and frequency domain results of the standard deviation of the displacement response at the center of gravity of pylon #2.

Multi-Mode Method								
	$\sigma_y(\text{m})$		$\sigma_z(\times 10^{-3} \text{ m})$		$\sigma_{\theta_x}(\times 10^{-3} \text{ rad})$		$\sigma_{\theta_y}(\times 10^{-3} \text{ rad})$	
	1.61		4.53		1.03		1.21	
Time Domain Method								
Realization	σ_y	Difference	σ_z	Difference	σ_{θ_x}	Difference	σ_{θ_y}	Difference
1	2.16	33.9%	6.09	34.3%	0.944	−8.63%	1.13	−8.68%
2	1.77	9.7%	4.50	10.1%	0.907	−12.2%	1.15	−7.8%
3	1.45	−9.84%	4.13	−8.79%	0.966	−6.5%	1.26	9.11%
4	2.00	24.4%	5.65	24.7%	0.961	−6.99%	1.17	0.17%
5	1.12	−30.5%	3.26	−28.0%	1.09	5.41%	1.20	−0.3%
Mean Value	1.70	5.53%	4.83	6.47%	0.973	−5.78%	1.18	−1.5%

Table 3

Standard deviation of the axial force in the tethers at the four corners of pylon #2.

	Corner 1	Corner 2	Corner 3	Corner 4
Linear	10.87	10.11	10.40	10.93
Geometric nonlinearity	10.73	9.99	10.27	10.82
Geometric nonlinearity and nonlinear buffeting forces	10.86	10.18	10.47	10.94

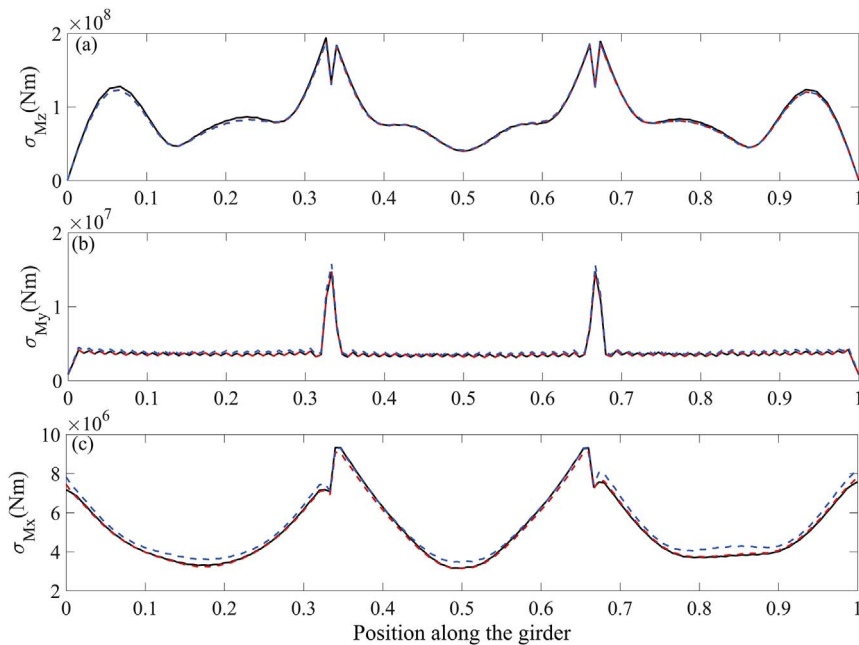


Fig. 11. Standard deviations of the section moment along the girder in the linearized and nonlinear system. (a) bending moment due to horizontal deflections; (b) bending moment due to vertical deflections; (c) torsional moment. The black solid line — represents the results in the linearized system; the dashed red line -- represents the results when considering geometric nonlinearities; and the blue dashed line -- represents the results considering both geometric nonlinearities and nonlinear buffeting forces. (For interpretation of the references to color in this figure legend, the reader is referred to the Web version of this article.)

3.5. Wind and wave contributions to the response of the bridge

In this section, different load combinations are considered to compare the relative influence of wind forces and first-order and second-order wave excitation forces. The load effects are calculated considering (i) only wind loads, (ii) wind loads and first-order wave excitation forces, and (iii) wind loads and first- and second-order wave excitation forces.

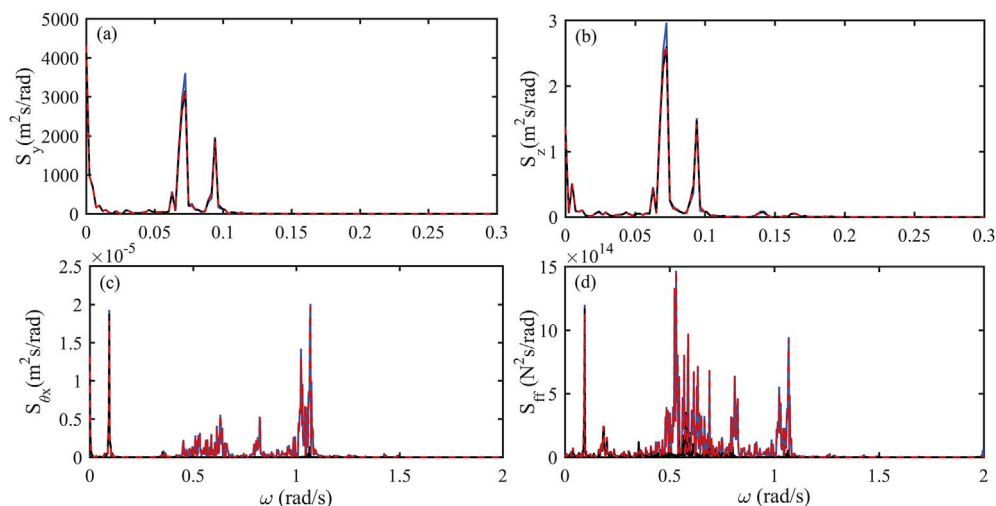


Fig. 12. Auto spectral density of the sway, heave and roll motion of pylon 2[#] and axial force in the tethers: (a) sway, (b) heave, (c) roll, (d) tether axial force. The black solid line — represents the results when there are only wind loads, the dashed red line --- represents the results when considering both wind loads and first-order wave excitation forces, and the blue solid line — represents the results considering wind loads and first- and second-order wave excitation force. (For interpretation of the references to color in this figure legend, the reader is referred to the Web version of this article.)

3.5.1. Pylons

Fig. 12 shows the auto spectral density of the sway, heave and roll motions of the pylon and the axial force in the tethers in one realization. The same time series are used in the cases of different load combinations. The low-frequency response is dominated by wind force, as the wind force is considerably larger in magnitude compared to the second-order difference frequency force (Fig. 9). Surprisingly, the second-order sum frequency force makes only a minimal difference to the response of the floating pylon and the axial force in the tethers in this case.

There are 2 peaks in the spectral density of the heave response at the same position of sway motion, as shown in Fig. 12(a) and (b), indicating that the heave motion is dominated by the coupling effect with sway. Fig. 12(c) shows that the roll motion is comprised of 2 components: one is produced by the coupling effect with wind-induced sway motion, and another is induced directly by the first-order wave force. In Fig. 12(d), the peaks on the power spectral density of the tether force are in good agreement with roll motion, which means that the tether force is mainly induced by roll motion instead of heave. Therefore, both wind and wave contribute to the axial force in the tethers; this is also observed in Table 4, showing similar contributions from wind and wave to the tether force under this environmental condition.

3.5.2. Girder

The standard deviations of the horizontal, vertical and torsional motions of the girder along with the corresponding auto spectral densities are presented in Fig. 13; the standard deviations of the corresponding section moments are presented in Fig. 14. The dynamic displacement response of the girder in the y-direction is mainly caused by the wind loading, and the effects from the first- and second-order wave forces are insignificant. However, the first-order wave excitation forces contribute significantly to the standard deviation of the bending moment due to horizontal deflections because the wave force can excite higher-order lateral natural modes, as can be observed in Fig. 13(b); higher modes yield higher curvature, which again provides high moments even if the response is small. The second-order wave excitation force has a minimal influence on the standard deviation of both the displacement response and section moments.

Table 4

Standard deviation of the axial force in the tethers at the corners of pylon #2: (i) only wind loads, (ii) wind loads and first-order wave excitation forces, (iii) wind loads and first- and second-order wave excitation forces.

Axial force in the tethers	Corner 1	Corner 2	Corner 3	Corner 4
Case i (MN)	5.11	4.90	5.06	5.00
Case ii (MN)	10.81	10.13	10.41	10.90
Case iii (MN)	10.86	10.19	10.48	10.94

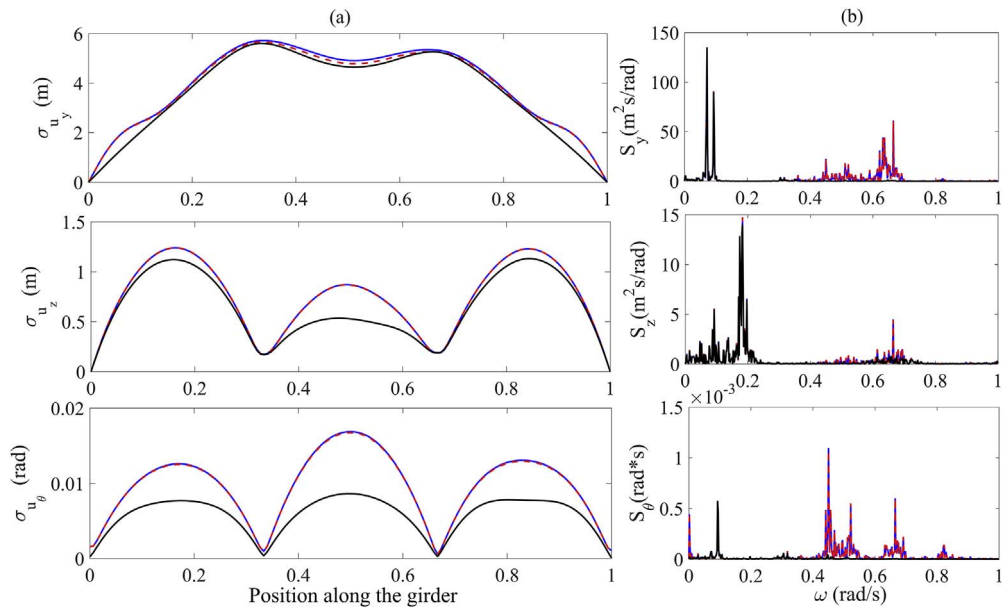


Fig. 13. (a) Displacement along the girder in the lateral, vertical and torsional directions; (b) auto spectral density of the displacement in the lateral, vertical and torsional directions. The line style and color representation are the same as in Fig. 12. (For interpretation of the references to color in this figure legend, the reader is referred to the Web version of this article.)

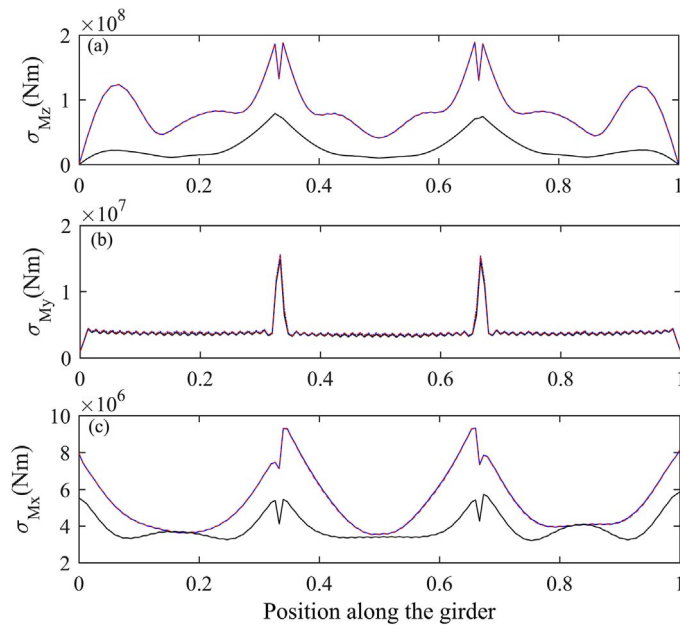


Fig. 14. Bending moments due to horizontal and vertical deflections and torsional moments along the girder. The line style and color representation are the same as in Fig. 12. (For interpretation of the references to color in this figure legend, the reader is referred to the Web version of this article.)

In the vertical direction, both the displacements and section moments are dominated by wind loading. No high-order modes are excited by the first- and second-order sum frequency forces, whereas high-order modes are observed in the spectral density of displacement for the torsional response. The amplitude of the high-mode response is larger than that in the y-displacement. However, in this high order mode, the girder deforms in all 3 directions, and torsional deformation is still a first-order mode shape. Therefore, the wave force contribution to the torsional moment is minimal compared to the contribution of the wave force to the bending moment.

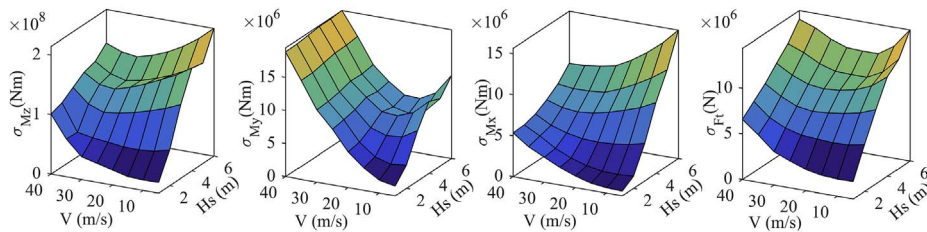


Fig. 15. Bending moments due to horizontal and vertical deflections and torsional moments in the most critical position of the girder and axial force in the tether under different wind velocities and wave heights.

3.6. Environmental parameter analysis

The variations in the standard deviation of the response of the bridge considering different significant wave heights and mean wind velocities are shown in Fig. 15. Considering only wind or waves, the load effects clearly increase with increases in the significant wave height and mean wind velocity. Conversely, the trends for combinations of both wind and waves are more complex, which can be seen for the bending moment due to horizontal deflections in the girder in Fig. 15. The standard deviation of the bending moment at high significant wave heights decreases as the mean wind velocity increases. This relationship is due to the self-excited aerodynamic forces changing the damping and stiffness of the system; in this case, the bending moment is reduced because the total damping for the horizontal motion increases. Similar trends are seen for the other load effects, which make it complicated to select the most severe combinations of the parameters for characterizing the environmental conditions.

4. Conclusions

This paper presents a study of the dynamic behavior of a three-span suspension bridge with two floating pylons subjected to wind and wave loads. The dynamic responses have been calculated in the time domain to study the influence of nonlinear effects and different load combinations on the model and to present some general trends of what it is important to include in the modeling of such a structure. Particular focus was placed on the efficient simulation of the aerodynamic self-excited forces and the hydrodynamic radiation forces using state space models.

The dynamic responses of a linearized model, i.e., the displacement of the girder and pylon, have been used to verify the presented time-domain methodology by comparing the obtained response statistics to the frequency domain results. The results illustrate that the time domain methodology accurately captures the dynamic behavior of the structure, as the time and frequency domain results are in good agreement. The computational efficiency is evaluated by comparing the time required in the cases with and without considering frequency-dependent forces. The former case takes 13% more computational time, which infers that the state-space model based time domain method is efficient.

The presented time domain method is then applied to the analysis of the nonlinear effects and the influence of wind and wave actions. It shows that geometric nonlinearities and second-order wave force have only a minimal influence for the particular case considered. However, only the one parameter Pierson-Moskowitz spectrum has been applied in this study, and the influence of the second-order wave loads should be further investigated considering several wave height and peak period combinations. A screening of combinations of significant wave heights and mean wind velocities illustrates that the section moment increases monotonically with the wave height. However, the trend is more complex for increasing mean wind velocities, as the properties of the system are altered due to the aerodynamic self-excited forces; the complexities make it challenging to select the combinations of the environmental parameters to be used in the design of the components of the structure.

Acknowledgements

This research was conducted with financial support from the Norwegian Public Roads Administration. The authors gratefully acknowledge this support.

Appendix. Multi-mode theory

This appendix outlines the frequency domain calculation of the dynamic response of the three-span suspension bridge with two floating pylons. The steps are illustrated in Fig. A1, and a brief explanation is given below.

Structural modal analysis

1. The beams in the FE model define the structural system matrices \mathbf{M}_s and \mathbf{K}_s . Additionally, the frequency-independent added mass $\mathbf{M}_h(\infty)$, the hydrostatic stiffness \mathbf{K}_h , and the time-invariant mean wind force and mean drift force \mathbf{F}_{mean} and \mathbf{F}_{WA} , respectively, are included in the finite element model. The modes φ and frequencies ω are calculated, and the system is transformed to generalized coordinates. $\tilde{\mathbf{M}}_0$, $\tilde{\mathbf{C}}_0$, and $\tilde{\mathbf{K}}_0$ denote the generalized mass, damping and stiffness matrices, respectively.

Aerodynamics

2. The aerodynamic damping and stiffness matrices in modal coordinates, $\tilde{\mathbf{C}}_{ae}$ and $\tilde{\mathbf{K}}_{ae}$, respectively, are calculated using the mode shapes obtained in step 1 [5].
3. \mathbf{B}_q contains the force coefficients of the girder and $\mathbf{S}_v^+(\Delta x, \Delta z, z, \omega)$ represents the cross spectral densities matrix of the turbulent velocity components of the wind field at two points, as illustrated in Eq. (17). $\tilde{\mathbf{S}}_{Buff}$ is the generalized buffeting force spectrum [5].

Hydrodynamics

4. \mathbf{m}_h and \mathbf{c}_h are the frequency-dependent hydrodynamic added mass and damping, respectively. As in step two, these matrices must be transformed to generalized coordinates, $\tilde{\mathbf{M}}_h$ and $\tilde{\mathbf{C}}_h$.
5. $\mathbf{T}^{(1)}(\omega, \theta)$ represents the transfer function for the first-order wave excitation forces, which is equal for both floating pylons, $\mathbf{T}_1^{(1)}(\omega, \theta) = \mathbf{T}_2^{(1)}(\omega, \theta)$. Here, subindices 1 and 2 refer to the first and second pylons, respectively. $S_\eta(\omega, \theta)$ is the auto-spectral density of the water elevation at the position of the pylons.

\mathbf{S}_p contains the cross-spectral densities of the first-order wave excitation forces acting on the two floating pylons and is transformed into generalized coordinates $\tilde{\mathbf{S}}_p$ [45].

6. $\mathbf{T}^{(2\pm)}(\omega_1, \omega_2, \theta_1, \theta_2)$ is the full quadratic transfer functions for the second-order sum and difference frequency force, as discussed in Chapters 2.3.2 and 2.3.3. The cross-spectral densities of the second-order wave forces of the two floating pylons have not been considered ($\mathbf{S}_{p_{ij}}^{2\pm} = 0 (i \neq j)$). The derivation of $\mathbf{S}_{p_{ii}}^{2\pm}$ is provided in Ref. [36]. $\tilde{\mathbf{S}}_p^{2\pm}$ represents the second-order wave excitation force spectrum in generalized coordinates.

Response calculation

7. The total generalized system matrices are established by summing the contribution from the structure, the aerodynamics and the hydrodynamics. These matrices are used to establish the generalized transfer function $\tilde{\mathbf{H}}(\omega)$.
8. The cross-spectral density matrix is calculated in generalized coordinates $\tilde{\mathbf{S}}_u(\omega)$.
9. The response is transformed from generalized to physical degrees of freedom $\mathbf{S}_u(\omega, x)$.

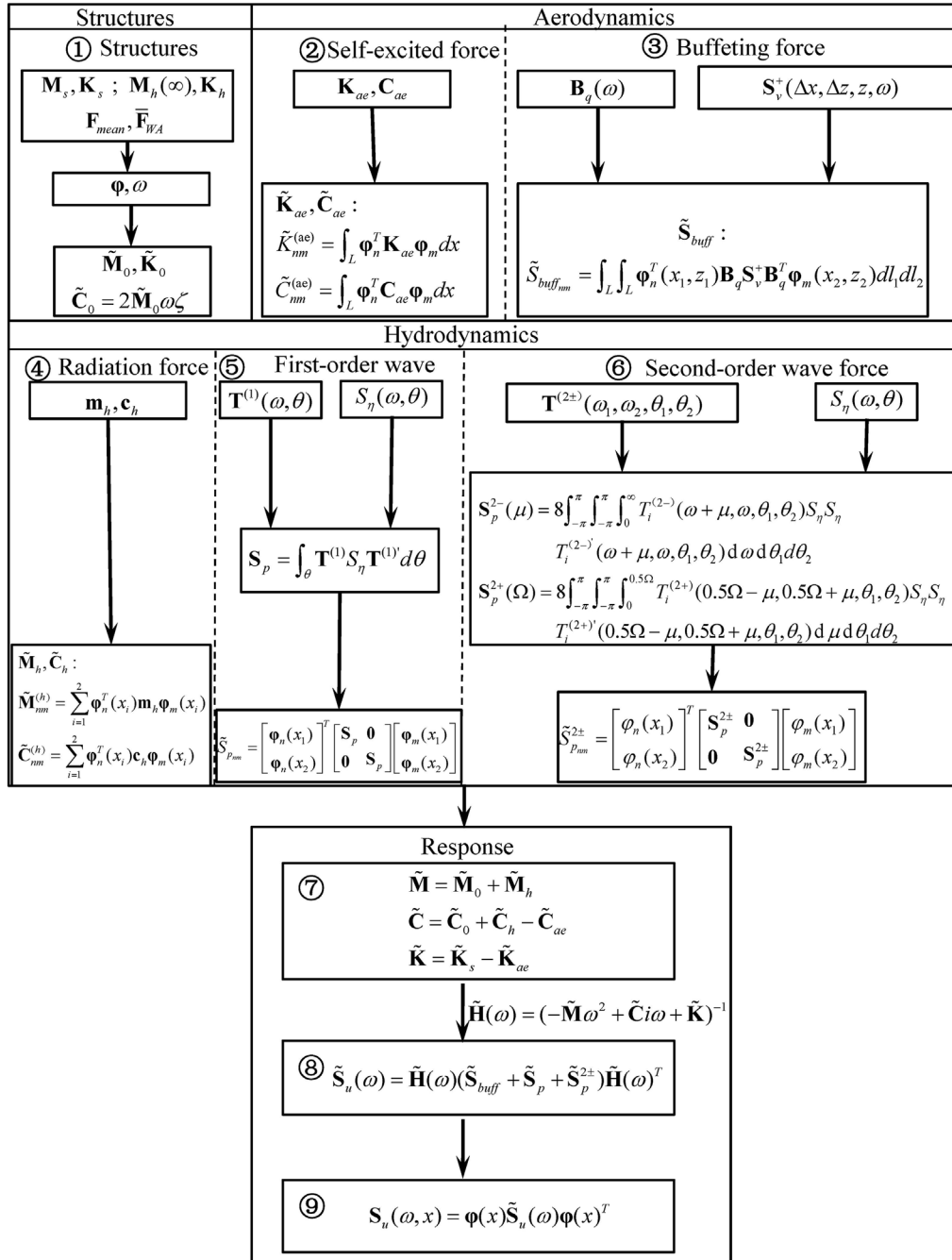


Fig. A.1. Theory of the multimode method.

References

- [1] Fredriksen AG, Bonnemaire B, Lie H, Munkeby J, Næstebø A, Buckholm P, et al. Comparison of global response of a 3-span floating suspension bridge with different floater concepts. ASME 2016 35th international conference on ocean, offshore and arctic engineering: american society of mechanical engineers. 2016. V007T06A66–VT06A66.
- [2] Veie J, Holtberget S. Three span floating suspension bridge crossing the Bjørnafjord. Multi-Span Large Bridges. International conference on multi-span large bridges, 1-3 july 2015. Porto, Portugal: CRC Press; 2015. p. 373.
- [3] Borri C, Costa C. Quasi-steady analysis of a two-dimensional bridge deck element. Comput Struct 2004;82:993–1006.
- [4] Diana G, Bruni S, Cigada A, Collina A. Turbulence effect on flutter velocity in long span suspended bridges. J Wind Eng Industrial Aerodynamics 1993;48:329–42.
- [5] Øiseth O, Rønnquist A, Sigbjørnsson R. Simplified prediction of wind-induced response and stability limit of slender long-span suspension bridges, based on

- modified quasi-steady theory: a case study. *J wind Eng industrial aerodynamics* 2010;98:730–41.
- [6] Scanlan RH, Tomko J. Air foil and bridge deck flutter derivatives. *J Soil Mech Found Div* 1971;97(6):1717–37.
 - [7] Theodorsen T. General theory of aerodynamic instability and the mechanism of flutter. *NACA Rep* 1935;496:413–33.
 - [8] Garrick IE. On some reciprocal relations in the theory of nonstationary flows. *NACA Tech Rep* 1938;629.
 - [9] Wagner H. Über die Entstehung des dynamischen Auftriebes von Tragflügeln. *ZAMM-Journal Appl Math Mechanics/Zeitschrift für Angewandte Math und Mech* 1925;5:17–35.
 - [10] Roger KL. Airplane math modelling methods for active control design. *Structural Aspects of Control. AGARD Conf Proceeding* 1977;9:4.1–4.11.
 - [11] Borri C, Costa C, Zuhlten W. Non-stationary flow forces for the numerical simulation of aeroelastic instability of bridge decks. *Comput Struct* 2002;80:1071–9.
 - [12] Salvatori L, Spinelli P. Effects of structural nonlinearity and along-span wind coherence on suspension bridge aerodynamics: some numerical simulation results. *J Wind Eng Industrial Aerodynamics* 2006;94:415–30.
 - [13] Chen X, Kareem A. Aeroelastic analysis of bridges under multicorrelated winds: integrated state-space approach. *J Eng Mech* 2001;127:1124–34.
 - [14] Chen X, Matsumoto M, Kareem A. Time domain flutter and buffeting response analysis of bridges. *J Eng Mech* 2000;126:7–16.
 - [15] Øiseth O, Rønnquist A, Sigbjørnsson R. Finite element formulation of the self-excited forces for time-domain assessment of wind-induced dynamic response and flutter stability limit of cable-supported bridges. *Finite Elem Analysis Des* 2012;50:173–83.
 - [16] Holappa KW, Falzarano JM. Application of extended state space to nonlinear ship rolling. *Ocean Eng* 1998;26:227–40.
 - [17] Cummins W. The impulse response function and ship motions. *DTIC Document*. 1962.
 - [18] Kashiwagi M. Transient responses of a VLFS during landing and take-off of an airplane. *J Mar Sci Technol* 2004;9:14–23.
 - [19] Wu M, Moan T. Linear and nonlinear hydroelastic analysis of high-speed vessels. *J Ship Res* 1996;40:149–63.
 - [20] Taghipour R, Perez T, Moan T. Hybrid frequency–time domain models for dynamic response analysis of marine structures. *Ocean Eng* 2008;35:685–705.
 - [21] Taghipour R, Perez T, Moan T. Time-domain hydroelastic analysis of a flexible marine structure using state-space models. *J Offshore Mech Arct Eng* 2009;131:011603.
 - [22] Fossen TI. A nonlinear unified state-space model for ship maneuvering and control in a seaway. *Int J Bifurcation Chaos* 2005;15:2717–46.
 - [23] Kristiansen E, Hjulstad Å, Egeland O. State-space representation of radiation forces in time-domain vessel models. *Ocean Eng* 2005;32:2195–216.
 - [24] Faltinsen O. Sea loads on ships and offshore structures. Cambridge university press; 1993.
 - [25] Diana G, Rocchi D, Belloli M. Wind tunnel: a fundamental tool for long-span bridge design. *Struct Infrastructure Eng* 2015;11:533–55.
 - [26] Øiseth O, Rønnquist A, Sigbjørnsson R. Time domain modeling of self-excited aerodynamic forces for cable-supported bridges: a comparative study. *Comput Struct* 2011;89:1306–22.
 - [27] Xu Y, Øiseth O, Naess A, Moan T. Prediction of long-term extreme load effects due to wind for cable-supported bridges using time-domain simulations. *Eng Struct* 2017;148:239–53.
 - [28] Petersen ØW. Model-based stochastic-deterministic State and force estimation using Kalman filtering with application to Hanko-1 channel marker Master thesis NTNU 2014.
 - [29] Shinozuka M. Monte Carlo solution of structural dynamics. *Comput Struct* 1972;2:855–74.
 - [30] Shinozuka M, Jan C-M. Digital simulation of random processes and its applications. *J sound Vib* 1972;25:111–28.
 - [31] Strømmen E. Theory of bridge aerodynamics. Springer Science & Business Media; 2010.
 - [32] Journée J, Massie W. Offshore hydromechanics: TU delft. 2000.
 - [33] Sharma JN, Dean RG. Second-Order directional seas and associated wave forces. *Society of Petroleum Engineers*; 1981. p. 129–40.
 - [34] Pierson WJ, Moskowitz L. A proposed spectral form for fully developed wind seas based on the similarity theory of SA Kitaigorodskii. *J Geophys Res* 1964;69:5181–90.
 - [35] Longuet-Higgins MS, Cartwright D, Smith N. Observations of the directional spectrum of sea waves using the motions of a floating buoy. *Proc Conf Ocean Wave Spectra*. Prentice-hall; 1963. p. 111–32.
 - [36] Pinkster J. The influence of directional spreading of waves on mooring forces. *Offshore technology conference*. 1988. Offshore technology conference.
 - [37] Pinkster JA. Low frequency second order wave exciting forces on floating structures: TU Delft. Delft University of Technology; 1980.
 - [38] Marthinsen T, Winterstein SR. Second-order load and response statistics for tension-leg platforms. *Rep RMS-9, Rel Marine Struc Prog*. 1992.
 - [39] Gong SW, Halden S. Dynamic response of suspension bridge with floating towers: master thesis NTNU. 2016.
 - [40] Lee C-H. WAMIT theory manual: Massachusetts institute of technology, department of ocean engineering. 1995.
 - [41] Perez T, Fossen TI. A matlab toolbox for parametric identification of radiation-force models of ships and offshore structures. *Model Identif Control* 2009;30:1.
 - [42] Siedziako B, Øiseth O, Rønnquist A. An enhanced forced vibration rig for wind tunnel testing of bridge deck section models in arbitrary motion. *J Wind Eng Industrial Aerodynamics* 2017;164:152–63.
 - [43] Li Y, Liao H, Qiang S. Simplifying the simulation of stochastic wind velocity fields for long cable-stayed bridges. *Comput Struct* 2004;82:1591–1598.
 - [44] Hansen SO. The hardanger bridge: static and dynamic wind tunnel tests with a section model. 2009.
 - [45] Kvåle KA, Sigbjørnsson R, Øiseth O. Modelling the stochastic dynamic behaviour of a pontoon bridge: a case study. *Comput Struct* 2016;165:123–35.